

## Enhancement of a fire detection algorithm by eliminating solar reflection in the mid-IR band: application to AVHRR data

LIMING HE<sup>†‡</sup> and ZHANQING LI<sup>\*†§</sup>

<sup>†</sup>Department of Atmospheric and Oceanic Science, Earth System Science

Interdisciplinary Center, University of Maryland, College Park, MD 20740, USA

<sup>‡</sup>Department of Geography and Program in Planning, University of Toronto, Toronto, ON, Canada M5S 3G3

<sup>§</sup>State Laboratory of Earth Surface Process and Resource Ecology, College of Global Change and Earth System Science, Beijing Normal University, Beijing 100875, PR China

(Received 1 November 2011; in final form 26 May 2012)

Satellite data from the Advanced Very High Resolution Radiometer (AVHRR) have been widely employed for fire monitoring around the world by virtue of the thermal emission in the middle-infrared (mid-IR) channel at 3.7  $\mu\text{m}$ . This channel, however, receives both thermal emission and solar reflection. As far as fire detection is concerned, the solar reflection contaminates the fire emission signal, which can cause significant errors, especially over non-forest biomes. This study presents a method to detect and eliminate the significant contribution of solar reflection to the AVHRR mid-IR band so that the fire detection accuracy is improved. AVHRR data from April to November 2004 were analysed. Twenty-seven percent of commission errors, mainly located in the southwestern part of North America, were found to be caused by the strong solar reflection from the surface. We also found that the calculated solar reflection itself is an effective indicator of false detections for the AVHRR. Introducing a new test to take into account this effect leads to a considerable reduction in commission errors. The new filter can eliminate most commission errors at the expense of minor increases in omission errors. The total number of true fires is missed by 0.3%, and the total number of false fire detections is reduced by 27.1%.

### 1. Introduction

Fire is one of the driving factors in global ecosystem patterns and processes, through its alteration of vegetation distribution and structure, global carbon balance, and climate (Bowman *et al.* 2009). Smoke from fires (Li *et al.* 2001b) can drastically alter the surface radiation budget (SRB) (Li 1998), which needs to be accounted for in the retrieval of SRB from satellite (Masuda *et al.* 1995). The spatial distribution of fires, which can be detected from satellites, is increasingly emerging as an important input to earth system models (Ju and Chen 2008). Advanced Very High Resolution Radiometer (AVHRR) data (Cihlar *et al.* 1997, Cracknell 1997) from National Oceanic and Atmospheric Administration's (NOAA) polar orbiting satellites have played an important role in wildfire detection over the last two decades

---

\*Corresponding author. Email: zli@atmos.umd.edu

(Lee and Tag 1990, Cahoon *et al.* 1994, Flasse and Ceccato 1996, Justice *et al.* 1996, Li *et al.* 1997, Giglio and Kendall 1999, Pu *et al.* 2007). For example, the Fire Identification, Mapping and Monitoring Algorithm (FIMMA) product from an operational system of fire detection at the NOAA employs daily AVHRR data to detect fires across the United States (<http://www.ssd.noaa.gov/PS/FIRE/Layers/FIMMA/fimma.html>).

Although various fire detection algorithms were proposed (Giglio and Kendall 1999, Li *et al.* 2001a, Xu *et al.* 2010) for eliminating false fires caused by satellite noise, clouds, hot surfaces, sun glint (Khattak *et al.* 1991) and so on, those algorithms still suffer from the fundamental problems of solar contamination and saturation in the middle-infrared (mid-IR) band (Cracknell 1997), which are the major sources of commission errors, especially in non-forest areas (Li *et al.* 2001a, He and Li 2011). A recent study of fire detection using Moderate Resolution Imaging Spectroradiometer (MODIS) data (He and Li 2011) showed that moderate improvements can be achieved in the detection rate while retaining low commission errors by eliminating the solar contamination.

In this study, we continue to improve fire detection by eliminating solar contamination in the mid-IR band using AVHRR data and the FIMMA. An earlier method proposed by He and Li (2011) exploited the corrected brightness temperature (BT) in the mid-IR band after the solar reflection was eliminated. However, given that the saturation temperature (330 K) in the AVHRR mid-IR band is very low and about half of all hotspots are saturated, the same method (He and Li 2011) cannot be applied to AVHRR data directly because it is difficult to distinguish if any pixels are saturated due to the contribution of thermal emission from fires, or the solar contamination, or both. Thus, a removal of solar contamination for saturated pixels may underestimate the thermal emission and introduce extra errors. Instead of using BT, we directly input the reflected solar radiation received by the AVHRR into the FIMMA by introducing a new filter, in order to improve the accuracy of the fire detection algorithm by means of the removal of false fire detections.

## 2. Data sets and method

The data and methodology employed for eliminating false detections caused by solar radiation for AVHRR data are described in the following subsections.

### 2.1 Data sets

AVHRR (NOAA-15, 16, and 17) data covering North America (NA) from April to November 2004 were provided by the NOAA/Coast Watch sector ([http://www.class.noaa.gov/saa/products/search?datatype\\_family=AVHRR](http://www.class.noaa.gov/saa/products/search?datatype_family=AVHRR)). The data are geo-corrected and operationally used in the Hazard Mapping System (HMS) at NOAA (McNamara *et al.* 2004, Stephens *et al.* 2005, Schroeder *et al.* 2008). The AVHRR bands are described in table 1.

The MODIS Land Surface Temperature/Emissivity Monthly L3 Global 0.05Deg CMG product (MOD11C3, collection 4) generated for 2003 (Wan and Li 1997, Petitcolin and Vermote 2002) was used to derive surface emissivity for AVHRR mid-IR bands. The emissivity in MODIS band 20 (3.66–3.84  $\mu\text{m}$ ) was used because it is the closest to AVHRR band 3b.

The MOD12Q1 V004 Land Cover product (Friedl *et al.* 2002) was used in the FIMMA. We employed the 14-class system developed at the University of Maryland

Table 1. Summary of daytime AVHRR fire detection algorithms and modifications (definitions of the variables are given in the notes below).

| No. | Components (filters)                               | Criteria and thresholds   | References  |
|-----|--|---|---|
| 1   | Cloud masking                                      | $(\rho_1 + \rho_2 > 1.2)$ or $(T_5 < 265 \text{ K})$ or $(\rho_1 + \rho_2 > 0.8$ and $T_5 < 285 \text{ K})$   | Saunders and Kriebel (1988); Stroppiana <i>et al.</i> (2000)          |
| 2   | Potential fire identification                      | $T_3 > \max(T_{3i} + 10, 306 \text{ K})$ and $\Delta T > 8 \text{ K}$ and $T_4 > 260 \text{ K}$ and $\rho_1 < 0.3$ and $\rho_2 < 0.3$   | Stroppiana <i>et al.</i> (2000); Giglio and Kendall (1999)            |
| 3   | Single hot spot filtering                          | $N_f < 1$   | Li <i>et al.</i> (2000)   |
| 4   | Eliminate fires in noisy data                      | A set of filters to eliminate false fires around bad scanned lines, barcode pattern, noisy data; exclude any fires in the first and last 350 scan lines   | Li <i>et al.</i> (2000)   |
| 5   | Reject fires in water, bare ground and urban areas | By land-cover product: 0, 12 or 13  | Li <i>et al.</i> (2000)   |
| 6   | Sun glint rejection 1                              | $\rho_2 > 0.25$ and $ \theta_s - \theta_v  < 50^\circ$  | Li <i>et al.</i> (2000)   |
| 7   | Sun glint rejection 2                              | $\theta_g < 32^\circ$   | Giglio <i>et al.</i> (2003)   |
| 8   | Sun glint rejection 3                              | $ \rho_1 - \rho_2  < 0.03$ and $N_{aw} \geq 1$  | Stroppiana <i>et al.</i> (2000)                                       |
| 9   | Contextual test                                    | $\Delta T > \max(0, \overline{\Delta T}) + \max(4 \cdot \delta_{\Delta T}, 6 \text{ K})$ and $T_3 > \overline{T}_3 + (11 \text{ K or } 16 \text{ K})$ and $(T_4 > \overline{T}_4 + \delta_{T_4} - 2 \text{ K})$ | Lee and Tag (1990); Prins and Menzel (1992); Justice and Dowty (1994) |
| 10  | Filter false fires with large solar contamination  | $((L_s > 0.14$ and $T_4 < 313 \text{ K})$ or $T_4 \geq 313 \text{ K})$ and $NDVI < 0.2$   | This study  |

Notes:  $\rho_1$  and  $\rho_2$  are bidirectional reflectance factors for AVHRR band 1 (0.65  $\mu\text{m}$ ) and band 2 (0.86  $\mu\text{m}$ ).  $T_3$ ,  $T_4$  and  $T_5$  are BTs for band 3 (3.75  $\mu\text{m}$ ), band 4 (10.8  $\mu\text{m}$ ) and band 5 (12  $\mu\text{m}$ ), respectively.

The original algorithm was applied to all daytime measurements with an SZA ( $\theta_s$ ) less than  $90^\circ$ . In our study, 'daytime' is limited to  $\theta_s \leq 75^\circ$ , which posed a major problem due to the strong solar reflection.  $\rho_1$  and  $\rho_2$  are not corrected for the SZA effect.  $T_{3i}$  is the mean of  $T_{3j}$  for lines  $i-50$  through  $i+50$  ( $T_{3i}$  is the mean  $T_3$  of any valid background pixels in line  $i$ ).  $N_f$  is the number of potential fires within the adjacent Right pixels.  $\Delta T = T_3 - T_4$ ;  $\overline{\Delta T}$  and  $\delta_{\Delta T}$  are the respective mean and mean absolute deviations of  $\Delta T$ ;  $\overline{T}_4$  and  $\delta_{T_4}$  are the respective mean and mean absolute deviations of  $T_4$ ; and  $\overline{T}_4$  and  $\delta_{T_4}$  are the respective mean and mean absolute deviations of  $T_4$ . In filter 7,  $\cos \theta_g = \cos \theta_v \cos \theta_s - \sin \theta_v \sin \theta_s \sin \theta_\phi$ , where  $\theta_v$  and  $\theta_s$  are the viewing zenith angle and SZA, and  $\phi$  is the relative azimuth angle.  $N_{aw}$  is the number of water pixels within the  $11 \times 11$  window surrounding the tentative fire pixel. Any pixels in the background window for statistics with ( $T_3 > 320 \text{ K}$  or  $\Delta T > 20 \text{ K}$ ) are assumed to be fire pixels and are excluded from the statistics.  $NDVI = (\rho_2 - \rho_1)/(\rho_1 + \rho_2)$ . In filter 9, 16 K is for land-cover categories (8) through (11), and 11 K is for the other valid land-cover categories.

(Hansen *et al.* 2000): water (0), evergreen needleleaf forest (1), evergreen broadleaf forest (2), deciduous needleleaf forest (3), deciduous broadleaf forest (4), mixed forest (5), woodland (6), wooded grassland (7), closed shrubland (8), open shrubland (9), grassland (10), cropland (11), bare ground (12) and urban and built-up (13).

Surface elevation data at a spatial resolution of 30 seconds are from the US Geological Survey (<http://edc.usgs.gov/products/elevation/gtopo30/gtopo30.html>). The solar contamination is attenuated by the atmosphere and explained by the surface elevation in the algorithm.

The fire detection results were compared with human-added hotspots confirmed by the accompanying smokes by the analysts who inspected Geostationary Operational Environmental Satellite (GOES) and AVHRR imageries, which are a subset of the HMS fire data from April to November 2004. The HMS is an interactive system in which satellite analysts manually integrate, inspect, and filter fire data generated from various automated fire detection algorithms. Using active fire data detected from GOES and polar orbiting satellite (AVHRR and MODIS) imagery, quality-controlled products of fire locations and major smoke plumes are generated for NA (McNamara *et al.* 2004, Stephens *et al.* 2005). The quality of HMS data is validated against coincident Advanced Spaceborne Thermal Emission and Reflection Radiometer (ASTER) data (Schroeder *et al.* 2007). It was found that hotspots added by analysts are reliable; however, some true fires detected by automated algorithms may be wrongly deleted because they lack discernible smoke plumes. The validation study revealed that commission errors from the MODIS and GOES fire products are less than 2% and omission errors are up to 80% or more over the United States (most of the omission errors owing to the big difference in spatial resolutions between the ASTER and the MODIS). As such, we employed the original MODIS and GOES fire products (i.e. including those data filtered out by the HMS) together with hotspots added by analysts, as ground truth to test the FIMMA. Given that the combined fire products may still not detect some real fires, we try to maintain the same level of omission errors while modifying the fire detection algorithm.

## 2.2 The method

**2.2.1 The original FIMMA.** In this study, the original FIMMA forms the basis for developing a new filter. The FIMMA was based on the scheme described in Li *et al.* (2000) and implemented as a contextual algorithm, taking advantage of several fire detection algorithms (Giglio and Kendall 1999, Li *et al.* 2001a). Additional filters were added to screen for noisy data. The daytime algorithm is summarized in table 1. The original FIMMA is composed of filters 1–9. Filter 1 is used to mask out cloudy pixels. The BT ( $T_b$ ) is converted from total radiance ( $L$ ) received in a mid-IR band,

$$T_b = B'(L) \quad (1)$$

where  $B'(L)$  represents the inversion function of Planck's law. Filter 2 is used to differentiate potential fire pixels from hot ground. Any single hot spot (i.e. none of its adjacent 8 pixels are potential fires) from filter 2 is doubtful because of noise and thus is excluded in filter 3. Filter 4 is used to eliminate false fires around badly scanned lines, barcode patterns and so on. Thermal anomalies such as pixels in water, bare

ground and urban areas (checked using the land-cover product) are excluded in filter 5. Filters 6–8 are used to exclude sun glint from bright backgrounds (e.g. soil and water) around their specular reflection directions. Filter 9 is composed of a series of contextual threshold tests that look for pixels that have distinctly higher mid-IR BTs ( $T_3$ ) and BT differences ( $\Delta T = T_3 - T_4$ ) than their non-fire background. In filter 9, valid non-burning neighbouring (or the background) pixels are searched for from a  $5 \times 5$  up to a  $41 \times 41$  window around a potential fire pixel until at least 35% of the pixels within the window are valid background pixels and the number of valid background pixels is at least eight.

**2.2.2 The new filter.** The radiance received in a mid-IR channel under clear-sky conditions consists of two parts: the thermal emission,  $L_t$ , from the atmosphere and ground surface, and the solar reflection,  $L_s$ , resulting from the scattering/reflection of the atmosphere and surface (Wan and Li 1997). In this study, we created filter 10 (table 1) to reduce commission errors in the accounting of  $L_s$  and the Normalized Difference Vegetation Index (NDVI):

$$((L_s > A \text{ and } T_4 < Bk) \text{ or } T_4 \geq Bk) \text{ and } NDVI < C \quad (2)$$

where  $A$ ,  $B$  and  $C$  are thresholds to be determined. The surface bidirectional reflectance factor (or directional emissivity) in the mid-IR band is needed to accurately calculate  $L_s$  (Tang *et al.* 2009). The only operational emissivity product for the mid-IR band, the global MODIS Land Surface Temperature/Emissivity product (Wan 2008), is based on the assumption that the surface is a Lambertian surface (Wan and Li 1997). We used this product and adopted the same assumption. Omitting angle notations for simplification,  $L_s$  can be expressed as

$$L_s = L_p + \frac{\alpha}{\pi(1 - \alpha \cdot S)} \cdot \mu_s \cdot E_0 \cdot [t_s + t_{ds}] \cdot [t_v + t_{dv}]. \quad (3)$$

where  $L_p$  is the path radiance resulting from the scattering of solar radiation by the atmosphere;  $\alpha$  is the surface albedo;  $S$  is the spherical albedo of the atmosphere;  $\mu_s$  is the cosine of the solar zenith angle (SZA);  $E_0$  is the solar irradiance incident at the top of the atmosphere (normal to the beam);  $t_s$  is the transmission function for the solar beam;  $t_{ds}$  is the transmission function for downward diffuse solar radiation;  $t_v$  is the direct transmission function between the surface and the sensor and  $t_{dv}$  is the transmission function for the upward diffuse solar radiation. The parameter  $\alpha$  is related to the surface emissivity as  $\alpha = 1 - \varepsilon$  according to Kirchhoff's law, and  $\varepsilon$  is acquired from the MODIS emissivity product (He and Li 2011). In simulating satellite-observed signals, radiances were integrated over the bandpass of the sensor weighted by the spectral response function of the sensor (<http://www2.ncdc.noaa.gov/docs/klm/>).

The components of  $L_s$  ( $L_p$ ,  $S$ ,  $t_s$ ,  $t_v$ ,  $t_{ds}$  and  $t_{dv}$ ) are computed using the MODTRAN4 model (Berk *et al.* 1998) with a variety of atmospheric parameters and varying viewing geometries (including surface elevation) for the NOAA-15, 16 and 17 AVHRR mid-IR bands. The output data are then used to develop look-up tables (LUTs) for speedy application. Multi-dimensional linear interpolation is performed to estimate any of the six parameters.

In order to choose thresholds  $A$ ,  $B$  and  $C$  in equation (2), we have analysed the ranges of  $L_s$ ,  $T_4$  and NDVI for original FIMMA-detected false fires, which were distinguished by the ‘ground truth’ data set described in section 2.1.

### 3. Results and discussion

#### 3.1 Determination of thresholds for the new filter

Figure 1 shows the increase in BT ( $\Delta T = B'(L_t + L_s) - B'(L_t)$ ) for varying  $L_t$  (BT along the  $x$ -axis) and  $L_s$  for AVHRR channel 3b (N16). It illustrates that the higher the ratio of  $L_s/L_t$ , the higher the increase in BT. A high  $L_s$  can cause a significant increase in BT, which could trigger the fire alarm.

AVHRR data from July 2004 were used to determine thresholds for filter 10. After applying the original FIMMA (filters 1–9) to AVHRR data from this month, 33,674 hotspots were detected, of which 1695 (5.0%) were false fires. The percentage of false fires is low because forest fires dominate in this month and the FIMMA performs well in detecting such fires. The reason for selecting data from July as training data is that for this year, the greatest number of fires occurred in July and the solar contamination was stronger than other months except June.

Strong solar contamination occurs at either small SZAs or small viewing zenith angles (VZAs) (short path lengths), whereas large  $L_p$  occurs at either larger SZAs or larger VZAs (long path lengths).  $L_p$  is generally only several hundredths of the total  $L_s$  except for those pixels with very low albedos; the stronger the solar contamination, the lower the proportion of  $L_p$ . Of the 33,674 fire pixels, only 2556 (7.6%) pixels have  $L_s$  larger than  $0.1 \text{ W m}^{-2} \text{ sr}^{-1} \mu\text{m}^{-1}$ , and  $L_p$  comprises only  $2.2 \pm 1.2\%$  of the  $L_s$ . To improve the computation efficiency,  $L_p$  is omitted in the calculation of  $L_s$ .

In order to choose threshold  $A$  for  $L_s$  in the detection of false fires, we used a scatter plot of  $L_s$  and  $T_4$  to separate false fires (red) from true fires (blue), as shown in figure 2.

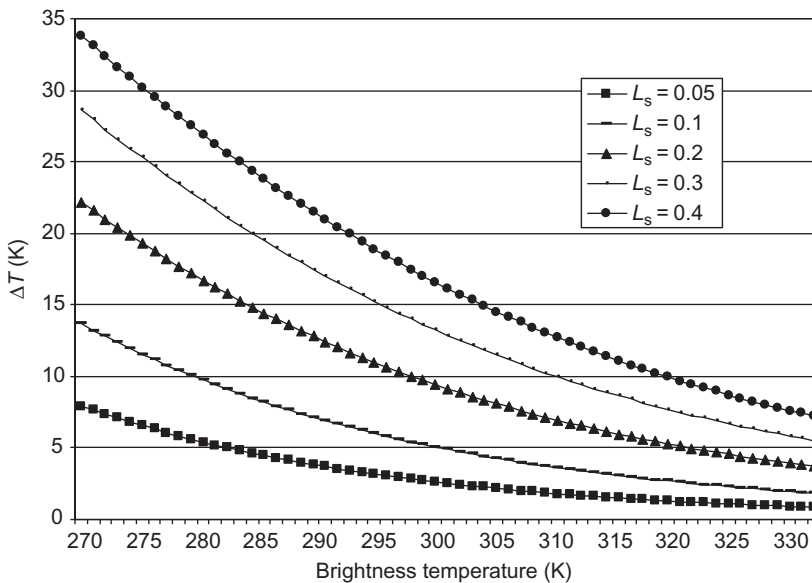


Figure 1. The increase in BT ( $\Delta T = B'(L_t + L_s) - B'(L_t)$ ) with varying  $L_s$  and  $L_t$  (or BT).

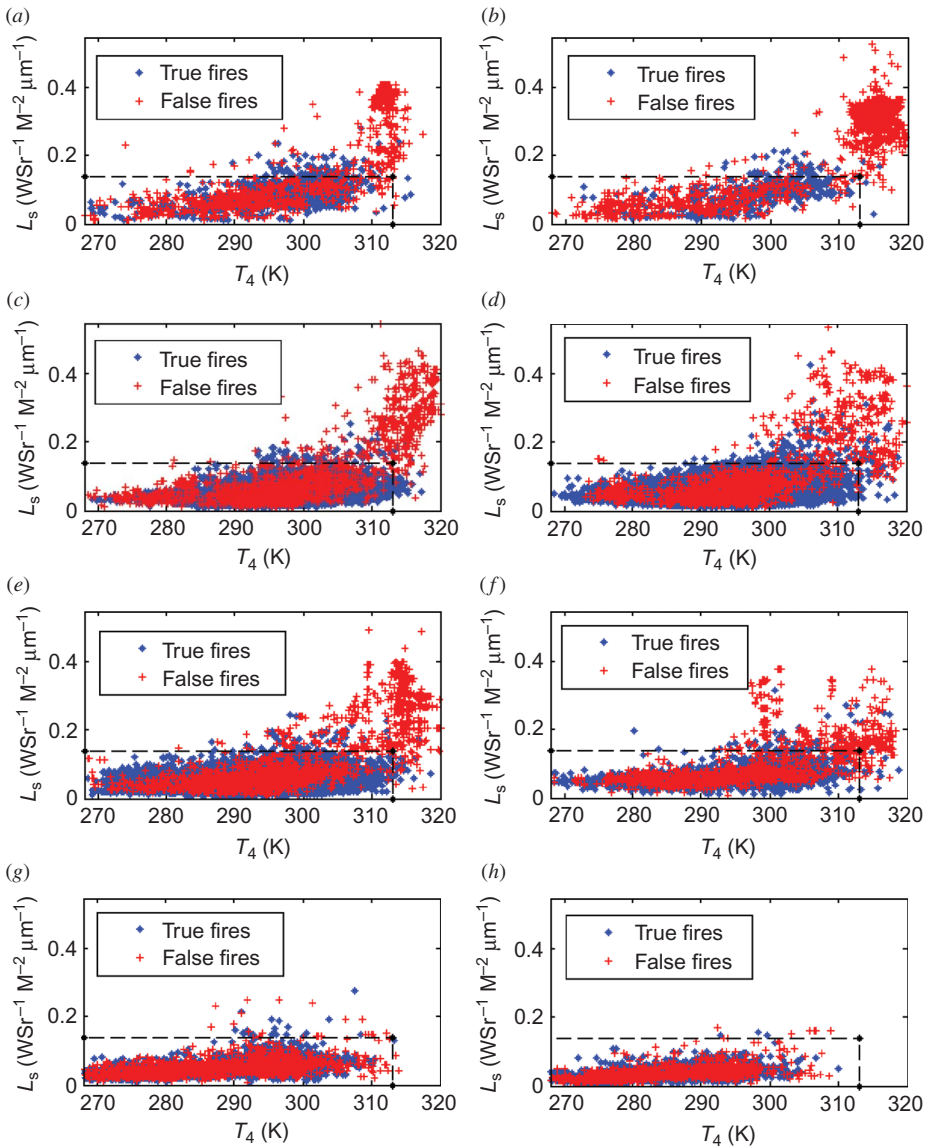


Figure 2. Scatter-plots of  $T_4$  and  $L_s$  for hotspots in 2004. (a) April, (b) May, (c) June, (d) July, (e) August, (f) September, (g) October and (h) November.

We chose  $T_4$  because it never saturates for any fire pixels from the FIMMA. The dashed line in figure 2 is selected to single out most of the false fires caused by solar contamination, while retaining the vast majority of true fires. The horizontal line (for threshold  $A$ ) in figure 2 is set at  $0.14 \text{ W m}^{-2} \text{ sr}^{-1} \mu\text{m}^{-1}$ . The vertical line (threshold  $B$ ) in figure 2 is  $313 \text{ K}$ ; this value was chosen because from the analysis of true fire pixels data in July 2004, few true fire pixels have  $T_4 > 313 \text{ K}$ . If a fire pixel from filter 9 has a  $\text{NDVI} > 0.2$  (threshold  $C$ ), this pixel is more likely to be a fire pixel (Kalpomeni and Kudoh 2006). Thus, in this study, any fire pixels with  $\text{NDVI} > 0.2$  are identified as true fires in filter 10 regardless of the magnitude of  $L_s$ .

### 3.2 The result

The new filter was validated using an independent set of data, namely 7 months worth of AVHRR data. The performance of filter 10 is summarized in table 2. The ‘ground truth’ refers to the number of fire pixels in the validation data set; ‘true’ and ‘false’ are the numbers of true fires and false fires identified by the validation data set. The commission error ( $C$ , in %) is defined as the ratio of the number of false fire pixels detected by the AVHRR to the number of AVHRR fire pixels during a month and is expressed as a percentage. The omission error ( $O$ , in %) is defined as the difference between the sum of fire pixels in the validation data set and the AVHRR (FIMMA) fire pixels and the total number of fire points in the validation data set.

Comparing output from the original FIMMA and the new version, commission errors decrease substantially, whereas omission errors remain roughly the same. The total number of false fires is reduced by 27.1% with or without applying filter 10 (from 11,593 to 8454, or by 3139). Meanwhile, the number of true fires decreases by only 326 (from 102,792 to 102,466) or 0.31%. Of the 3139 false fires eliminated by filter 10, a total number of 2295 pixels (or 73.1%) are in the ‘open shrublands’ category, 332 pixels (or 10.6%) are in the ‘wooded grassland’ category, 178 (5.7%) pixels are in the ‘grassland’ category, 151 pixels (or 4.8%) are in the ‘woodland’ category and 131 pixels (or 4.2%) are in the ‘closed shrublands’ category. The biomass in these land-cover types is generally low and the reflectance in the mid-IR band is high.

Table 2 and figure 2 show that the solar contamination effect in October and November is much less than in other months because of the much weaker contribution of solar radiation. In general, commission errors and omission errors are small for forest fires and large for agricultural fires, which are mainly located in the southern part of the United States.

Figure 3 is a demonstration of the performance of the new filter in the FIMMA for July 2004. False fires eliminated by filter 10 are shown as dots. Most of the false fires induced by solar contamination and eliminated by filter 10 are in the south western region of NA. An inspection of Google Earth® images shows that the typical landscape here contains a low amount of biomass resulting in high reflectance, which causes such commission errors (e.g. in the lower right panel of figure 3, where the geographic coordinate is 32.640° N, 106.073° W).

Table 2. Summary of validation results.

|           | Ground truth | Original FIMMA (without filter 10) |        |      |      | New FIMMA (with filter 10) |       |      |      |
|-----------|--------------|------------------------------------|--------|------|------|----------------------------|-------|------|------|
|           |              | True                               | False  | O%   | C%   | True                       | False | O%   | C%   |
| April     | 25,969       | 1,120                              | 989    | 95.7 | 46.9 | 1,092                      | 602   | 95.8 | 35.5 |
| May       | 15,936       | 492                                | 1,592  | 96.9 | 76.4 | 467                        | 495   | 97.1 | 51.5 |
| June      | 59,831       | 22,799                             | 1,716  | 61.9 | 7.0  | 22,730                     | 1,266 | 62.0 | 5.3  |
| July      | 92,797       | 31,979                             | 1,695  | 65.5 | 5.0  | 31,857                     | 1,344 | 65.7 | 4.0  |
| August    | 69,299       | 35,255                             | 1,712  | 49.1 | 4.6  | 35,211                     | 1,244 | 49.2 | 3.4  |
| September | 25,709       | 3,562                              | 1,247  | 86.1 | 25.9 | 3,535                      | 888   | 86.2 | 20.1 |
| October   | 22,983       | 4,794                              | 1,490  | 79.1 | 23.7 | 4,786                      | 1,468 | 79.2 | 23.5 |
| November  | 22,968       | 2,791                              | 1,152  | 87.8 | 29.2 | 2,788                      | 1,147 | 87.9 | 29.1 |
| Total     | 335,492      | 102,792                            | 11,593 | 69.4 | 10.1 | 102,466                    | 8,454 | 69.5 | 7.6  |



Figure 3. Demonstration of the performance of the new filter in the FIMMA. False fires eliminated by filter 10 are shown as dots. These false fires mainly occurred in the southwestern part of NA because there is less vegetation thus high solar reflection in this region. The period covered is April–November 2004.

### 3.3 Discussion

Like any other filters, thresholds  $A$ ,  $B$ , and  $C$  in filter 10 may be tuned according to specific satellite, region, emissivity data quality and even application objectives. The spectral response functions for AVHRR 3 (NOAA-15, 16 and 17) are close enough to void any adjustment. In this study, the algorithm is trained using fire data in July in the NA covering various land-cover types and performs well in three seasons. In the light of the physical basis for the corrections, these thresholds may not be modified for other seasons when fires are not very intensive and solar contamination is weak, let alone being much less. Of course, they may be fine-tuned for applications over small regions with ground truth data available to improve fire detection accuracy.

To detect false fires, filter 10 relies on  $L_s$  that is partly based on the MODIS emissivity product, which assumes a Lambertian surface. This assumption is useful to reduce the number of unknowns in the inversion algorithm (Wan and Li 1997). A comparison of the MODIS emissivity product (Wan 2008) and the retrieved emissivity from bidirectional reflectance distribution function (BRDF) models showed that their differences (root mean square error = 0.024) are not significant (Tang *et al.* 2009). As such, we also assume that the surface is a Lambertian surface when calculating  $L_s$ . This assumption and the quality of the MODIS emissivity product influence the performance of the new filter. For example, if  $L_s$  is underestimated, a false fire may not pass the test in filter 10; true fires may pass the test if  $L_s$  is overestimated.

To improve the performance of this filter in the long run, the MODIS emissivity product should be improved, which in turn will improve the accuracy of  $L_s$ . It should also be realized that there is a trade-off between commission errors and omission errors, for example, the user can choose to increase the threshold for  $L_s$  in order to decrease omission errors with the cost of increasing commission errors in their application.

In an operational fire detection system, the timely MODIS emissivity and land-cover products are unavailable due to the lag in their processing. For this reason, we have designed to detect fire for the current year by using land cover and emissivity from the previous year. MODIS emissivity data (from July 2003) and MODIS land-cover data (for 2003) used for the calculation of  $L_s$  in July 2004 were outdated; so there may be extra errors in  $L_s$ , especially for areas where the land cover undergoes significant changes.

#### 4. Concluding remarks

The FIMMA is in operational use by the NOAA for detecting fires automatically using AVHRR data covering NA. A quality-controlled fire product is also generated by the supervised integration of multiple fire products from AVHRR, MODIS and GOES through the HMS (McNamara *et al.* 2004, Stephens *et al.* 2005). Satellite-detected fire hot spots are validated by apparent smoke plumes that could be detected automatically (Li *et al.* 2001b). Validation against ASTER fire data (Schroeder *et al.* 2007) indicated that the overwhelming majority of fires detected by MODIS and GOES data are true fires (99%), although some fires were wrongly deleted because they had such faint smoke plumes. On the other hand, fires with discernible smoke plumes that go undetected by satellite sensors were added by analysts. As such, both MODIS and GOES fire products, combined with human-added fires as ground truth, are employed in this study.

AVHRR data are widely used in fire detection, but there exist two outstanding issues: saturation of the mid-IR channel and contamination of thermal emission by solar reflection (Li *et al.* 2001b). The saturation problem prevents us from using the corrected BT to improve fire detection after the solar reflection is eliminated, as proposed by He and Li (2011). Analysis of false fires detected by the original FIMMA shows that high solar reflection leads to some false detections. This can be lessened by removing the solar reflection.

To this end, an LUT is created for the calculation of reflected solar radiation in the AVHRR mid-IR band. A new test is proposed to reduce commission errors generated by the FIMMA. The performance of the revised FIMMA was tested using the aforementioned hybrid fire product. We find that the new test can eliminate a significant amount (27.1%) of commission errors caused by the solar contamination with a minor increase (<0.3%, depending on the month) in omission errors. Consistent results are obtained when the algorithm is applied to both the data sets used for algorithm development (July 2004) and for testing (April through June and August through November 2004). The majority of false fires occurred in the southwestern part of NA due to the low vegetation density and ensuing high solar reflection.

#### Acknowledgements

This study was supported by the NOAA GOES-R risk reduction project. The AVHRR data were downloaded from NOAA's Comprehensive Large Array-data Stewardship System (CLASS). The MODIS fire product was downloaded from the

MODIS web fire mapper. The GOES fire product was downloaded from the National Geophysical Data Center. The HMS data were downloaded from NOAA's National Environmental Satellite, Data, and Information Service (NESDIS). The authors thank I. Csiszar and W. Schroeder for their useful comments.

## References

- BERK, A., BERNSTEIN, L.S., ANDERSON, G.P., ACHARYA, P.K., ROBERTSON, D.C., CHETWYND, J.H. and ADLER-GOLDEN, S.M., 1998, MODTRAN cloud and multiple scattering upgrades with application to AVIRIS. *Remote Sensing of Environment*, **65**, pp. 367–375.
- BOWMAN, D.M.J.S., BALCH, J.K., ARTAXO, P., BOND, W.J., CARLSON, J.M., COCHRANE, M.A., D'ANTONIO, C.M., DEFRIES, R.S., DOYLE, J.C., HARRISON, S.P., JOHNSTON, F.H., KEELEY, J.E., KRAWCHUK, M.A., KULL, C.A., MARSTON, J.B., MORITZ, M.A., PRENTICE, I.C., ROOS, C.I., SCOTT, A.C., SWETNAM, T.W., VAN DER WERF, G.R. and PYNE, S.J., 2009, Fire in the earth system. *Science*, **324**, pp. 481–484.
- CAHOON, D.R., STOCKS, B.J., LEVINE, J.S., COFER, W.R. and PIERSON, J.M., 1994, Satellite analysis of the severe 1987 forest-fires in Northern China and Southeastern Siberia. *Journal of Geophysical Research-Atmospheres*, **99**, pp. 18627–18638.
- CIHLAR, J., CHEN, J. and LI, Z., 1997, Seasonal AVHRR multichannel data sets and products for studies of surface-atmosphere interactions. *Journal of Geophysical Research-Atmospheres*, **102**, pp. 29625–29640.
- CRACKNELL, A.P., 1997, *The Advanced Very High Resolution Radiometer (AVHRR)* (London: Taylor & Francis).
- FLASSE, S.P. and CECCATO, P., 1996, A contextual algorithm for AVHRR fire detection. *International Journal of Remote Sensing*, **17**, pp. 419–424.
- FRIEDL, M.A., MCIVER, D.K., HODGES, J.C.F., ZHANG, X.Y., MUCHONEY, D., STRAHLER, A.H., WOODCOCK, C.E., GOPAL, S., SCHNEIDER, A., COOPER, A., BACCINI, A., GAO, F. and SCHAAF, C., 2002, Global land cover mapping from MODIS: algorithms and early results. *Remote Sensing of Environment*, **83**, pp. 287–302.
- GIGLIO, L. and KENDALL, J.D., 1999, Evaluation of global fire detection algorithms using simulated AVHRR infrared data. *International Journal of Remote Sensing*, **20**, pp. 1947–1985.
- GIGLIO, L., KENDALL, J.D. and MACK, R., 2003, A multi-year active fire dataset for the tropics derived from the TRMM VIRS. *International Journal of Remote Sensing*, **24**, pp. 4505–4525.
- HANSEN, M.C., DEFRIES, R.S., TOWNSHEND, J.R.G. and SOHLBERG, R., 2000, Global land cover classification at 1km spatial resolution using a classification tree approach. *International Journal of Remote Sensing*, **21**, pp. 1331–1364.
- HE, L. and LI, Z., 2011, Enhancement of fire detection algorithm by eliminating solar contamination effect and atmospheric path radiance: application to MODIS data. *International Journal of Remote Sensing*, **32**, pp. 6273–6293.
- JU, W.M. and CHEN, J.M., 2008, Simulating the effects of past changes in climate, atmospheric composition, and fire disturbance on soil carbon in Canada's forests and wetlands. *Global Biogeochemical Cycles*, **22**, GB3010, doi:10.1029/2007GB002935.
- JUSTICE, C.O., and DOWTY, P. (Eds.), 1994, IGBP-DIS satellite fire detection algorithm workshop technical report. IGBP-DIS Working Paper No. 9, 88 p., February 1993 (NASA/GSFC, Greenbelt, MD).
- JUSTICE, C.O., KENDALL, J.D., DOWTY, P.R. and SCHOLLES, R.J., 1996, Satellite remote sensing of fires during the SAFARI campaign using NOAA advanced very high resolution radiometer. *Journal of Geophysical Research-Atmospheres*, **101**, pp. 23851–23863.
- KALPOMA, K.A. and KUDOH, J.I., 2006, A new algorithm for forest fire detection method with statistical analysis using NOAA AVHRR images. *International Journal of Remote Sensing*, **27**, pp. 3867–3880.

- KHATTAK, S., VAUGHAN, R.A. and CRACKNELL, A.P., 1991, Sun glint and its observation in Avhrr data. *Remote Sensing of Environment*, **37**, pp. 101–116.
- LEE, T.F. and TAG, P.M., 1990, Improved detection of hotspots using the Avhrr 3.7- $\mu\text{m}$  channel. *Bulletin of the American Meteorological Society*, **71**, pp. 1722–1730.
- LI, Z., KAUFMAN, Y., ITHOKU, C., FRASER, R., TRISHCHENKO, A., GILGIL, L., JIN, J., YU, X., AHERN, F., GOLDAMMER, J.G. and JUSTICE, C., 2001a, A review of AVHRR-based fire active fire detection algorithm: principles, limitations, and recommendations. In *Global and Regional Vegetation Fire Monitoring from Space, Planning and Coordinated International Effort*, F. Ahern, J.G. Goldammer and C. Justice (Eds.), pp. 199–225 (The Hague: SPB Academic Publishing).
- LI, Z., NADON, S. and CIHLAR, J., 2000, Satellite-based detection of Canadian boreal forest fires: development and application of the algorithm. *International Journal of Remote Sensing*, **21**, pp. 3057–3069.
- LI, Z., 1998, Influence of absorbing aerosols on the inference of solar surface radiation budget and cloud absorption. *Journal of Climate*, **11**, pp. 5–17.
- LI, Z., CIHLAR, J., MOREAU, L., HUANG, F.T. and LEE, B., 1997, Monitoring fire activities in the boreal ecosystem. *Journal of Geophysical Research-Atmospheres*, **102**, pp. 29611–29624.
- LI, Z., KHANANIAN, A., FRASER, R.H. and CIHLAR, J., 2001b, Automatic detection of fire smoke using artificial neural networks and threshold approaches applied to AVHRR imagery. *IEEE Transactions on Geoscience and Remote Sensing*, **39**, pp. 1859–1870.
- MASUDA, K., LEIGHTON, H.G. and LI, Z.Q., 1995, A new parameterization for the determination of solar flux absorbed at the surface from satellite measurements. *Journal of Climate*, **8**, pp. 1615–1629.
- McNAMARA, D., STEPHENS, G., RUMINSKI, M. and KASHETA, T., 2004, The Hazard Mapping System (HMS) – NOAA’s multi-sensor fire and smoke detection program using environmental satellites. In *13th Conference on Satellite Meteorology and Oceanography*, 22 September 2004, Norfolk, VA.
- PETITCOLIN, F. and VERMOTE, E., 2002, Land surface reflectance, emissivity and temperature from MODIS middle and thermal infrared data. *Remote Sensing of Environment*, **83**, pp. 112–134.
- PRINS, E.M. and MENZEL, W.P., 1992, Geostationary satellite detection of biomass burning in South-America. *International Journal of Remote Sensing*, **13**, pp. 2783–2799.
- PU, R.L., LI, Z., GONG, P., CSISZAR, I., FRASER, R., HAO, W.M., KONDRAGUNTA, S. and WENG, F.Z., 2007, Development and analysis of a 12-year daily 1-km forest fire dataset across North America from NOAA/AVHRR data. *Remote Sensing of Environment*, **108**, pp. 198–208.
- SAUNDERS, R.W. and KRIEBEL, K.T., 1988, An improved method for detecting clear sky and cloudy radiances from Avhrr data. *International Journal of Remote Sensing*, **9**, pp. 123–150.
- SCHROEDER, W., RUMINSKI, M., CSISZAR, I., GIGLIO, L., PRINS, E., SCHMIDT, C. and MORISSETTE, J., 2007, Validation analyses of an operational fire monitoring product: the hazard mapping system. *International Journal of Remote Sensing*, **29**, pp. 6059–6066.
- SCHROEDER, W., RUMINSKI, M., CSISZAR, I., GIGLIO, L., PRINS, E., SCHMIDT, C. and MORISSETTE, J., 2008, Validation analyses of an operational fire monitoring product: the hazard mapping system. *International Journal of Remote Sensing*, **29**, pp. 6059–6066.
- STEPHENS, G., McNAMARA, D. and RUMINSKI, M., 2005, Operational fire and smoke monitoring in NESDIS’ satellite services division. *Earth Observation Magazine*, XIV.
- STROPPIANA, D., PINNOCK, S. and GREGOIRE, J.M., 2000, The global fire product: daily fire occurrence from April 1992 to December 1993 derived from NOAA AVHRR data. *International Journal of Remote Sensing*, **21**, pp. 1279–1288.
- TANG, B.H., LI, Z.L. and BI, Y.Y., 2009, Estimation of land surface directional emissivity in mid-infrared channel around 4.0  $\mu\text{m}$  from MODIS data. *Optics Express*, **17**, pp. 3173–3182.

- WAN, Z.M., 2008, New refinements and validation of the MODIS land-surface temperature/emissivity products. *Remote Sensing of Environment*, **112**, pp. 59–74.
- WAN, Z.M. and LI, Z.L., 1997, A physics-based algorithm for retrieving land-surface emissivity and temperature from EOS/MODIS data. *IEEE Transactions on Geoscience and Remote Sensing*, **35**, pp. 980–996.
- XU, W., WOOSTER, M.J., ROBERTS, G. and FREEBORN, P., 2010, New GOES imager algorithms for cloud and active fire detection and fire radiative power assessment across North, South and Central America. *Remote Sensing of Environment*, **114**, pp. 1876–1895.